

TWO-DIMENSIONAL NUMERICAL ANALYSIS OF ACTIVE FLOW CONTROL BY STEADY BLOWING ALONG FOIL SUCTION SIDE BY DIFFERENT URANS TURBULENCE MODELS

by

Jelena M. SVORCAN*, **Vasko G. FOTEV**, **Nebojša B. PETROVIĆ**,
and Slobodan N. STUPAR

Department of Aerospace Engineering, Faculty of Mechanical Engineering,
University of Belgrade, Belgrade, Serbia

Original scientific paper
<https://doi.org/10.2298/TSCI160126188S>

The effects of active separation control by steady blowing jets were investigated numerically on three different examples: subsonic flow past Aerospatiale A airfoil at 13° angle-of-attack, transonic flow past NACA 0012 airfoil at 4° angle-of-attack, and transonic flow in linear compressor/turbine cascade. Performed analyses are two-dimensional, flow is turbulent (or transitional) while fluid is viscous and compressible. Jets are positioned along the suction sides of the foils, the first one being located just upstream of the separation point, and modeled by source terms added to flow equations. Several different jet diameters and intensities are investigated. As the choice of turbulence model affects the final solution of Reynolds equations, turbulence is modeled by four different models: Spalart-Allmaras, realizable $k-\varepsilon$, $k-\omega$ SST, and $\gamma-Re_{\theta}$, and a comparison of obtained results is performed. Goals of the study include definition of an adequate numerical setting that enables sufficiently correct simulation of the problems in question as well as evaluation of the possible increase in aerodynamic performances. Lift coefficients, lift-to-drag ratios or relative pressure differences are improved for all controlled cases.

Key words: *computational aerodynamics, turbulence models, airfoil cascades, active boundary layer control, steady blowing*

Introduction

The computation of many engineering flow problems involving low Reynolds numbers (wind turbine blades), transition zones or complex rotational flows (helicopter and turbomachine blades) directly depends on the boundary layer modeling [1, 2]. Modern approaches assume computationally expensive hybrid RANS-LES, LES or DNS [3]. However, in practical problems where both computational economy and accuracy are equally important it is reasonable to use simpler models such as URANS equations closed by different turbulence models based on eddy viscosity [4-6]. Various possibilities exist, from one- to four-equation models, from fully turbulent to transitional boundary layer. In this study four different models were tested: Spalart-Allmaras, realizable $k-\varepsilon$, $k-\omega$ SST, and $\gamma-Re_{\theta}$.

* Corresponding author, e-mail: jsvorcan@mas.bg.ac.rs

Test cases involve three different airfoils: Aerospatiale A, classical NACA 0012, and NACA 8410 at quite different flow conditions ranging from transitional subsonic to transonic flows with both shock-induced and angle-of-attack-induced separation and unsteadiness. Two-dimensional simulations were performed in ANSYS FLUENT 16.2 [7, 8].

The ever-attractive problems of flow separation and active flow control that incorporate various complex flow phenomena and lie on the borderline of turbulence models applicability were studied. Main objectives of the research include determination of the abilities of different turbulence models to predict airfoil aerodynamic performances and their comparison (as well as qualitative estimation). In short, the ability of turbulence models to provide sufficiently accurate results (of complex flows) was tested. In order to determine the extent of both physical model errors and numerical errors, numerical results were compared to existing available experimental data [9-12].

Underlying principle of flow control is directing faster fluid particles towards the wall in order to overcome local adverse pressure gradients. It can be done in various ways, both passively and actively by adding mass, momentum, and additional energy to the flow. Usual solutions include slots or actuator jets, moving surfaces or plasma actuators [13-15]. Main advantages of flow control include avoiding or delaying separation, stabilizing boundary layer, delaying transition, reducing drag, increasing aerodynamic performance, *etc.* in both external and internal flows.

Although performed analyses are two-dimensional, they provide insight into possibilities to relatively easily simulate active flow control which has become an interesting and widely considered topic in recent years [16-21]. The increase of aerodynamic performances, achieved without the change of undisturbed velocity or angle-of-attack, is proven and quantified. Various jet configurations are tested and their efficiencies are compared. Finally, although such studies on subsonic flows around airfoils [16-19] and cascades [20] can be found, they have rarely been performed for transonic regimes [21].

Mathematical and numerical background

By decomposing flow quantities (solutions of Navier-Stokes equations) into mean and turbulent-fluctuation terms and assuming negligible fluctuations in viscosity μ and thermal conductivity λ , two-dimensional flow of viscous and compressible fluid is modeled by Reynolds equations (τ_{eff} – deviatoric stress tensor):

$$\frac{\partial \bar{\rho}}{\partial t} + \frac{\partial}{\partial x_j} (\bar{\rho} \bar{v}_j) = 0 \quad (1)$$

$$\frac{\partial}{\partial t} (\bar{\rho} \bar{v}_i) + \frac{\partial}{\partial x_j} (\bar{\rho} \bar{v}_i \bar{v}_j) = \rho \bar{F}_i - \frac{\partial \bar{p}}{\partial x_i} + \frac{\partial}{\partial x_j} \left[\mu \left(\frac{\partial \bar{v}_i}{\partial x_j} + \frac{\partial \bar{v}_j}{\partial x_i} - \frac{2}{3} \delta_{ij} \frac{\partial \bar{v}_k}{\partial x_k} \right) \right] + \frac{\partial}{\partial x_j} \left(-\overline{\rho v_i' v_j'} \right) \quad (2)$$

$$\frac{\partial}{\partial t} (\bar{\rho} \bar{E}) + \frac{\partial}{\partial x_j} [(\bar{\rho} \bar{E} + \bar{p}) \bar{v}_j] = \frac{\partial}{\partial x_j} \left[\left(\lambda + \frac{c_p \mu_t}{Pr_t} \right) \frac{\partial \bar{T}}{\partial x_j} + \bar{v}_i (\bar{\tau}_{ij})_{eff} \right] + S_h \quad (3)$$

In order to close and solve this system, it is necessary to define additional equations or in some way define turbulence scales. One of the computationally simplest approaches is to use Boussinesq viscosity hypothesis:

$$-\overline{\rho v_i' v_j'} = \mu_t \left(\frac{\partial \bar{v}_i}{\partial x_j} + \frac{\partial \bar{v}_j}{\partial x_i} \right) - \frac{2}{3} \left(\bar{\rho} k + \mu_t \frac{\partial \bar{v}_k}{\partial x_k} \right) \delta_{ij}, k = \frac{\overline{v'^2}}{2} = \frac{\overline{v_x'^2 + v_y'^2}}{2} \quad (4)$$

Turbulent viscosity μ_t is one of the flow characteristics and is determined from additional transport equations. Since no universally accepted turbulence model exists, here four different models were tried: one-equation Spalart-Allmaras (S-A), two-equation realizable $k-\varepsilon$ (real $k-\varepsilon$), two-equation $k-\omega$ SST, and four-equation $\gamma\text{-Re}_\theta$ (trans SST). Their additional equations are somewhat different [7].

One-equation Spalart-Allmaras model is a stable and reasonably accurate model for various classes of turbulent flows. Initially, it was developed for unstructured codes in aerospace industry but is also popular for turbomachinery applications. It incorporates modified turbulent viscosity equation:

$$\frac{\partial}{\partial t}(\rho \tilde{v}) + \frac{\partial}{\partial x_j}(\rho \tilde{v} v_j) = G_v + \frac{1}{\sigma_{\tilde{v}}} \left[\frac{\partial}{\partial x_j} \left((\mu + \rho \tilde{v}) \frac{\partial \tilde{v}}{\partial x_j} \right) + \rho C_{b2} \left(\frac{\partial \tilde{v}}{\partial x_j} \right)^2 \right] - Y_v \quad (5)$$

Modified turbulent viscosity equals 0 at walls, while solution variables are blended from their sublayer formulation to the corresponding logarithmic layer values.

Two-equation variant of $k-\varepsilon$ model, realizable $k-\varepsilon$ model, solves transport equations for turbulent kinetic energy k and its dissipation rate ε . There is a modified source term in the second equation:

$$\begin{aligned} \frac{\partial}{\partial t}(\rho k) + \frac{\partial}{\partial x_j}(\rho k v_j) &= \frac{\partial}{\partial x_j} \left[\left(\mu + \frac{\mu_t}{\sigma_k} \right) \frac{\partial k}{\partial x_j} \right] + \mu_t S^2 - \rho \varepsilon - 2 \rho \varepsilon \frac{k}{a^2} \\ \frac{\partial}{\partial t}(\rho \varepsilon) + \frac{\partial}{\partial x_j}(\rho \varepsilon v_j) &= \frac{\partial}{\partial x_j} \left[\left(\mu + \frac{\mu_t}{\sigma_\varepsilon} \right) \frac{\partial \varepsilon}{\partial x_j} \right] + \rho C_1 S \varepsilon - \rho C_2 \frac{\varepsilon^2}{k + \sqrt{\nu \varepsilon}} \end{aligned} \quad (6)$$

Turbulent viscosity is computed as $\mu_t = \rho C_\mu k^2/\varepsilon$. This variant generally exceeds the standard $k-\varepsilon$ model performance and it gives good results for complex flows (recirculation, separation, rotation, *etc.*). Enhanced wall treatment where domain is divided into viscosity-affected and fully-turbulent regions and flow in the viscosity-affected region is completely resolved all the way to the viscous sublayer was used.

Two-equation $k-\omega$ SST model presents a combination of standard $k-\omega$ model near the walls (since it is more accurate and numerically stable in the near wall region) and $k-\varepsilon$ model in the outer layer. It is generally more reliable than standard $k-\omega$ model. Transport equations for turbulent kinetic energy and its specific dissipation rate ω are:

$$\begin{aligned} \frac{\partial}{\partial t}(\rho k) + \frac{\partial}{\partial x_j}(\rho k v_j) &= \frac{\partial}{\partial x_j} \left[\left(\mu + \frac{\mu_t}{\sigma_k} \right) \frac{\partial k}{\partial x_j} \right] + \mu_t S^2 - \rho \beta^* k \omega \\ \frac{\partial}{\partial t}(\rho \omega) + \frac{\partial}{\partial x_j}(\rho \omega v_j) &= \frac{\partial}{\partial x_j} \left[\left(\mu + \frac{\mu_t}{\sigma_\omega} \right) \frac{\partial \omega}{\partial x_j} \right] + \frac{\alpha}{\nu_t} \mu_t S^2 - \rho \beta \omega^2 + D_\omega \left(\omega, \frac{\partial k}{\partial x_j}, \frac{\partial \omega}{\partial x_j} \right) \end{aligned} \quad (7)$$

Some constants differ for inner and outer layer, while the final term in the second equation appears only in the outer layer. Turbulent viscosity is computed as $\mu_t = \alpha^* \rho k/\omega$.

Four-equation γ - Re_θ model is particularly developed for transitional flows. It is derived from k - ω SST model with 2 additional equations for intermittency γ and momentum thickness Reynolds number Re_θ :

$$\begin{aligned} \frac{\partial}{\partial t}(\rho\gamma) + \frac{\partial}{\partial x_j}(\rho\gamma v_j) &= \frac{\partial}{\partial x_j} \left[\left(\mu + \frac{\mu_t}{\sigma_\gamma} \right) \frac{\partial \gamma}{\partial x_j} \right] + P_\gamma - E_\gamma \\ \frac{\partial}{\partial t}(\rho \text{Re}_\theta) + \frac{\partial}{\partial x_j}(\rho \text{Re}_\theta v_j) &= \frac{\partial}{\partial x_j} \left[\sigma_{\theta t} (\mu + \mu_t) \frac{\partial \text{Re}_\theta}{\partial x_j} \right] + P_{\theta t} \end{aligned} \quad (8)$$

The first equation determines the beginning of transition, while the second transmits the effects of outer layer flow into the boundary layer. Turbulent viscosity is computed as $\mu_t = \rho k / \omega$.

Numerical simulations were performed in ANSYS FLUENT 16.2 where mass, momentum, and energy conservation equations are solved by finite volume method [7, 8]. Fluid flow was considered as transient, and implicit density-based solver (where the governing equations are solved simultaneously and equations for additional scalars are solved afterwards) was used. Systems of linearized equations were solved by Gauss-Seidel scheme. Variable gradients were computed by Least Squares Cell-Based method. Spatial discretizations of flow quantities were second order upwind, while temporal discretizations were first order implicit. CFL number was set to 5, while the time-step order of magnitude was 10^{-3} s for airfoils and 10^{-4} s for cascades. Default values of under-relaxation factors were used. Additional explanations on the presented equations can be found in [7].

Flow around Aerospatiale A airfoil

In the first example a fully turbulent/transitional flow over an Aerospatiale A airfoil at Mach number $M = 0.15$, angle-of-attack $\alpha = 13.3^\circ$, and freestream Reynolds number $\text{Re} = 2 \cdot 10^6$ based on airfoil chord is solved. This configuration has been extensively researched, both experimentally and numerically, and presents one of the most used standard validation cases [9].

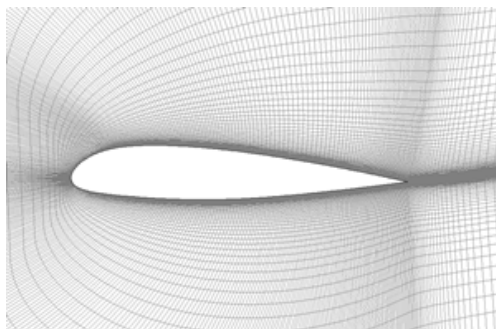


Figure 1. Computational grid around Aerospatiale A airfoil

Adopted numerical approach is quite orthodox. Computational grid is structured, planar, and extends from -18 to 25 airfoil lengths in x -direction and -18 to 21.56 airfoil lengths in y -direction, fig. 1. It comprises over 65000 quadrilateral cells with dimensionless wall distance $y^+ < 1$ and sharp trailing edge. Satisfactory mesh resolution in the boundary layer ($y^+ \approx 1$) enables the flow to be resolved all the way down to the wall. The mesh was not generated by the authors, but taken from available resources provided by ANSYS Inc. Dirichlet boundary conditions concerning velocity and pressure were imposed on inlet and outlet boundaries. No-slip boundary conditions were defined on airfoil surfaces.

Computed and measured pressure and skin friction coefficients graphs, C_p and C_f , respectively, are shown in fig. 2. Generally, the correspondence of pressure coefficient

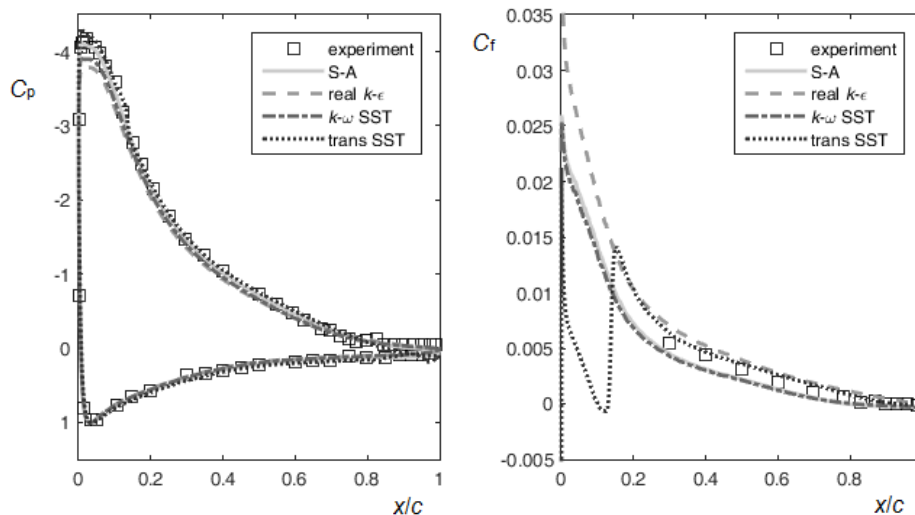


Figure 2. Pressure and skin friction coefficient distributions over Aerospatiale A airfoil

distributions (experimental vs. all four turbulent models) is satisfactory. Results obtained with realizable $k-\epsilon$ and $k-\omega$ SST mostly differ from experimental in the fore part of suction side.

Conclusions are not so straightforward with the skin friction coefficient. No data is available for the fore part of suction side where numerical results significantly differ. In accordance with its definition, transition $\gamma-Re_\theta$ model captures a small laminar separation bubble other models do not.

Flow around NACA 0012 airfoil

The classical NACA 0012 airfoil was chosen for its widespread and general usage. It is also a standard validation case, thoroughly tested both experimentally and numerically [10]. Chosen freestream flow conditions are $M = 0.82$ at $\alpha = 3.86^\circ$ and $Re = 9 \cdot 10^6$ with the separated flow following the supersonic bubble on the suction side, fig. 3. Angle-of-attack was not corrected using a linear method for simulating wind tunnel wall interference and was kept at a measured value of 3.86° . This case is a true test for turbulence models and it is difficult to achieve agreement with the corresponding experimental results obtained by Harris [11]. Although weakly transonic flow can successfully be computed, shock wave-boundary layer interaction still presents a computational challenge. Without adequate empirical relations or model coefficients adjustments it is almost impossible to obtain accurate solutions in this problematic region. Both computational shock wave strength and position do not coincide completely with the experimental. Moreover, grid refinement cannot bring significant improvement to results [10].

Although, in the previous example, air was considered as ideal gas and energy equation was solved, freestream Mach number was low. Results are more disperse when transonic regimes are simulated as can be seen from this example. Again, computational grid is planar, structured, and parabolic extending from -20 to 25 airfoil lengths in x -direction and -30 to 30 airfoil lengths in y -direction, fig. 4. Now it comprises over 50000 quadrilateral cells, with dimensionless wall distance $y^+ < 1$. Again, this classical mesh was taken from available resources provided by ANSYS Inc. Far-field values for static pressure, velocity components,

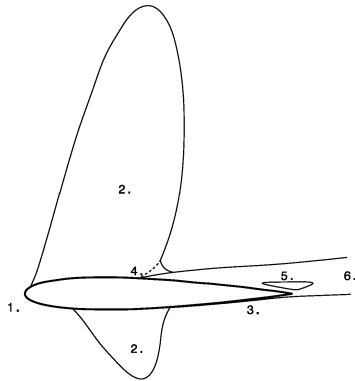


Figure 3. Different flow zones around NACA 0012 airfoil;
1. laminar boundary layer, 2. sonic bubble,
3. turbulent boundary layer, 4. separation
point, 5. separation region, 6. wake region

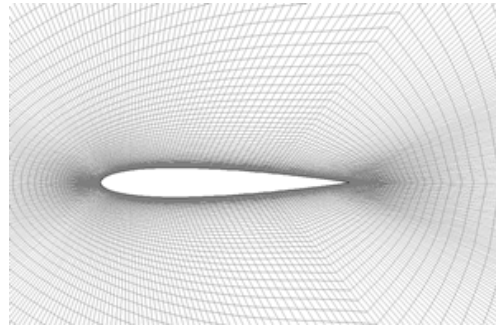


Figure 4. Computational grid around NACA 0012 airfoil

and turbulence quantities were defined on outer boundaries while no-slip boundary condition is imposed on the walls of the airfoil.

In order to compare four turbulence models, computed and measured pressure coefficient and skin friction coefficient graphs are formed, fig. 5. In this case the flow field is

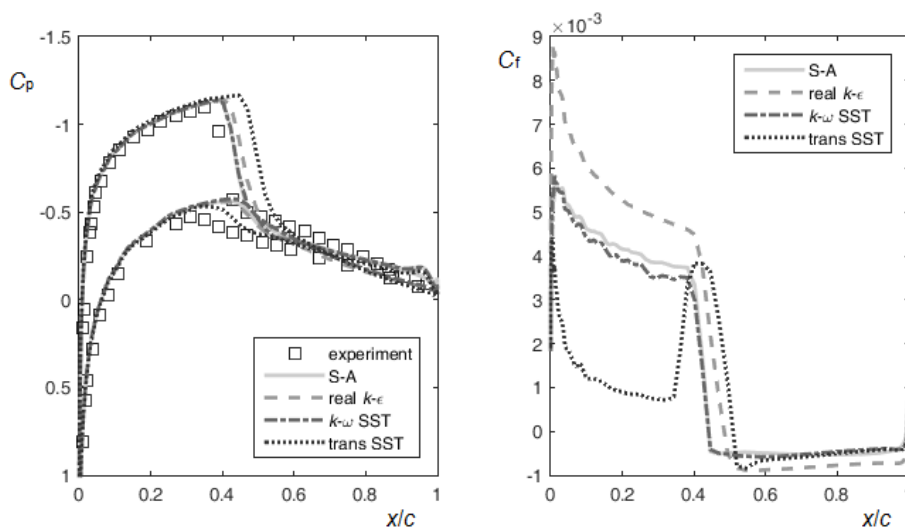


Figure 5. Pressure and skin friction coefficient distributions over NACA 0012 airfoil

complex with visible sonic zone, shock wave, thickening of the boundary layer, and flow separation captured by all four turbulence models, fig. 3. However, no model appears able to adequately simulate the shock wave-boundary layer interaction on the suction side. Greatest discrepancies in results appear immediately before and after the shock wave. Also, locations of the ending point of the sonic zone and separation point are computed differently by all

models. It can also be noted that skin friction coefficient distributions differ more than in the previous case of small Mach number with Spalart-Allmaras and $k-\omega$ SST models producing the most similar numerical values. Unfortunately, no experimental data is available for comparison.

Overall, grids of this size and density provide results of sufficient accuracy for the greatest number of engineering applications. They are also computationally inexpensive which makes them attractive for individual users and when fast, preliminary results are needed. However, it should be borne in mind that flow in critical zones may not be simulated adequately.

Flow in linear cascades

Tested compressor and turbine cascades geometries correspond to NACA 8410 airfoil at two different blade angles $\beta = 135^\circ$ and $\beta = 30^\circ$, respectively, fig. 6. Cascade solidity (ratio of distance between two adjacent profiles to their chord) in both configurations is 1. In accordance with the experimental data [12], flow in cascades for different flow angles α and inflow Mach numbers M_1 was simulated. Boundary conditions for the compressor configuration are $M_1 = 0.5$ at $\alpha = 148^\circ$ and $Re_2 = 3 \cdot 10^5$. For the turbine configuration they are $M_1 = 0.225$ at $\alpha = 70^\circ$ and $Re_2 = 5 \cdot 10^5$.

Computational grids are planar, quadrilateral, structured, and contain nearly 40000 cells, figs. 7 and 8. Again, dimensionless wall distance in both meshes is below one. These properties were adopted according to common practices and after a detailed grid convergence study and present a compromise between accuracy and simplicity necessary for further analysis.

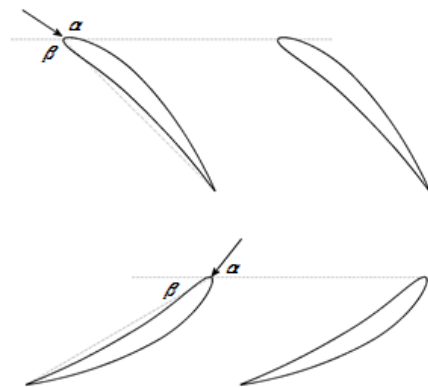


Figure 6. Model geometry: compressor and turbine configuration

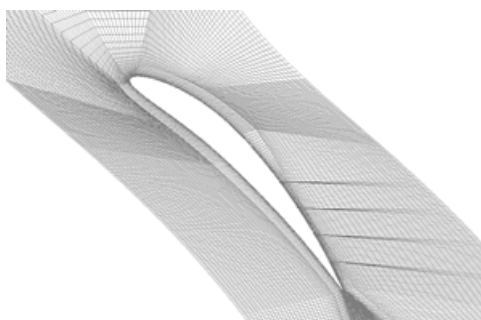


Figure 7. Grid around compressor cascade

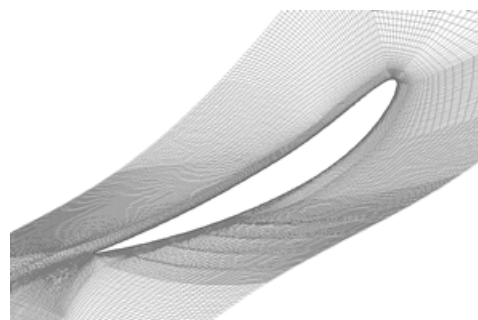


Figure 8. Grid around turbine cascade

The values of total and static pressure, velocity direction, and turbulent quantities (turbulence intensity $t = 1\%$, length scale $L = 0.003$ m, and intermittency $\gamma = 1$) are defined at the inlet boundary. At the outlet boundary only static pressure and turbulent quantities are set. The definition of the cascade is completed by a translational periodic boundary formed by the remaining two opposite boundary edges. This boundary condition can be used for fully-

developed periodic flows appearing with repeating geometry. It is always used in pairs and imposes the condition that the flow across two sides (or edges) is identical. Computationally, cells adjacent to the first and the opposite periodic boundary are treated as neighbors [7]. In this case, by applying periodic boundary condition, the interference between the airfoils in the cascade is taken into account and properly simulated.

Measured and computed pressure and skin friction coefficient distributions of the clean compressor model are shown in fig. 9. Although the general trend of the result seems to be reproduced the *compressor cascade* results notably differ from experimental, even along the pressure side of the foil. Even though various grids were tried the results remained around this level of accuracy, so the following short discussion is, in the first place, qualitative. Spalart-Allmaras and realizable $k-\epsilon$ provide most similar results, while results obtained by $k-\omega$ SST model differ the most. Again, transition $\gamma-Re_\theta$ model produces a laminar separation bubble. Also, while the other three models find similar positions of separation points, $k-\omega$ SST model results in the earliest separation.

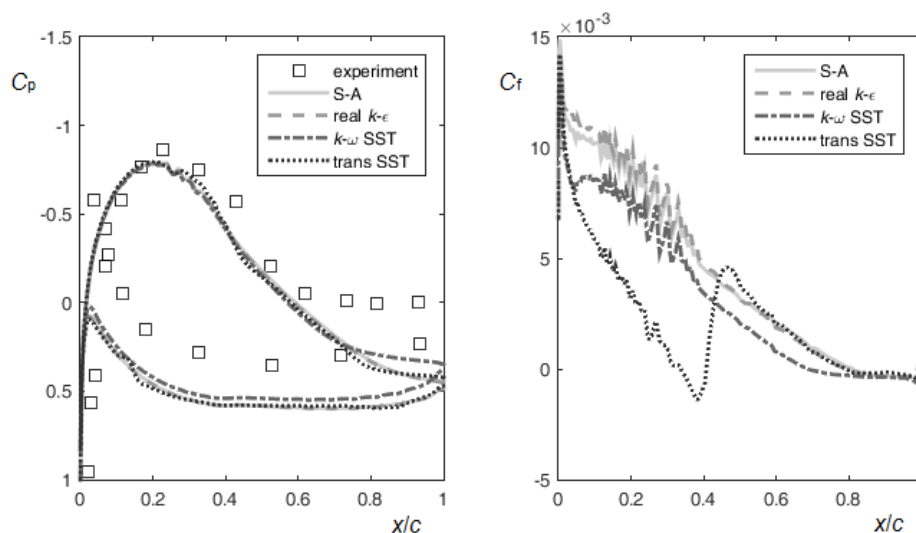


Figure 9. Pressure and skin friction coefficient distributions along the foil in compressor cascade

On the other hand, the *turbine cascade* seems easier to simulate. Significant discrepancies from experiment appear only in the critical zone of sonic zone-boundary layer interaction, fig. 10, while all numerical results generally coincide. By observing skin friction coefficient it can be concluded that again, $k-\omega$ SST model results in the earliest separation. Since the angle-of-attack is somewhat steep, laminar separation bubble appears at the nose of the foil with all models. However, its size differs depending on the used turbulence model, with realizable $k-\epsilon$ being the smallest and with $k-\omega$ SST and $\gamma-Re_\theta$ being the greatest.

Increase in aerodynamic performances by active flow control

Downturn in the pressure distribution at the suction side of the foil and negative values of wall shear stress are indicative of the flow separation. By injecting streams of fluid a fair degree of pressure recovery can be achieved, the separation point can be moved downward and the reattachment point can be moved upward. Therefore, after the definition of rela-

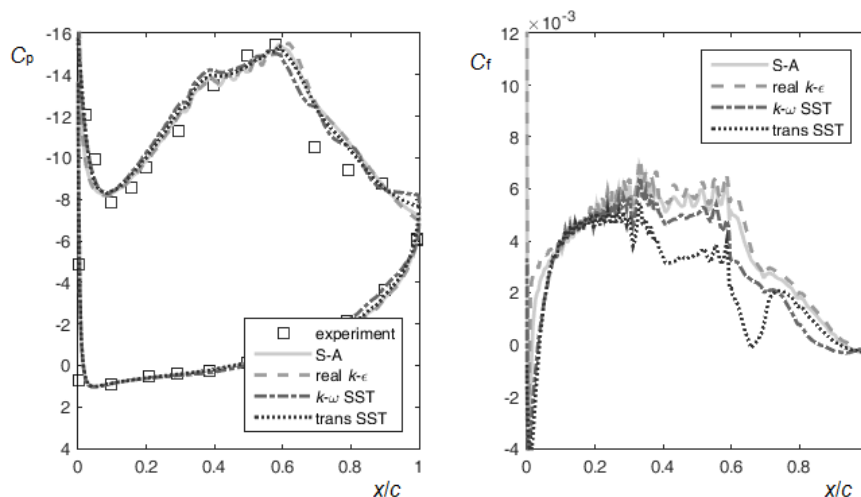


Figure 10. Pressure and skin friction coefficient distributions along the foil in turbine cascade

tively successful baseline numerical settings, the simulation of active boundary layer control by steady blowing was tried.

Among the numerous possible jet parameters two were chosen for further analysis: jet intensity B and orifice diameter D_j . In the first two cases jet intensity is defined as the ratio of jet and freestream Mach numbers, $B = M_{jet}/M$. In the third case, jet intensity is defined as the ratio of jet and inlet or outlet Mach numbers for compressor and turbine cascade, respectively, *i. e.* $B = M_{jet}/M_1$ or $B = M_{jet}/M_2$. Tested values of parameter B include 0.5, 1, and 2. Possible values of orifice diameter D_j are 0.25%, 0.5%, and 1% of the foil chord c .

Jet positions were defined for each model individually, and were not altered throughout computation. Four orifices were distributed equidistantly along the second half of the suction side of the blade, starting roughly from the separation point (since the location of the separation point differs slightly for every turbulence model). For the purpose of active flow control simulations the cells of the initial computational grids were not changed. The only modification made to the meshes was the creation of new zones that represent jets.

The effect of steady blowing is included into numerical flow solver by adding the jet mass flow, momentum, and energy sources into governing equations at newly created zones. The jet inflow is considered laminar. This computational approach is useful for significantly smaller sources than main flow inlet. It is also less complicated than generating a new, structured, locally refined grid for every new flow case [8], although it requires a density-based solver for purposes of accuracy. This approach to modeling different types of boundary layer control devices is common, [14]. The values of added source terms are functions of flow Mach number M , jet intensity B , and orifice diameter D_j .

Prior to the discussion of obtained results, it should be noted that numerical results of active flow control cases could not be confirmed by experiment (no suitable test cases were found). Furthermore, simultaneous visualizations and measurements of boundary layer parameters are rarely freely available. Therefore, the purpose of presented results is primarily for comparison and illustration of certain interesting phenomena.

Effects of steady blowing in the first two cases (of freestream flow) were quantified by aerodynamic performances – lift and drag coefficients, C_l and C_d . Since numerical results

with steady blowing obtained by different turbulence models differ only slightly, presented analyses for various combinations of jet parameters were computed using only one turbulence model that appeared to produce the most accurate results in the considered cases. For flows over Aerospatiale A the authors chose the transition γ - Re_θ model. Aerodynamic coefficients computed on the clean configuration are $C_l = 1.578$ and $C_d = 0.0189$, resulting in lift-to-drag ratio of $C_l/C_d = 83.65$. Computed aerodynamic coefficients with active flow control are listed in tabs. 1 and 2. It appears that an increase in jet intensity B is followed by increased lift coefficient regardless of jet diameter D_j , while drag coefficient is reduced only if orifice is sufficiently large. On the other hand, an increase in jet diameter reduces both coefficients ultimately resulting in even negative values of drag coefficient C_d . For a right combination of parameters it is possible to achieve significantly improved lift-to-drag ratio. Differences in Mach number contours for clean and optimal configuration based on the greatest computed lift-to-drag ratio ($B = 1, D_j = 0.01c$) are shown in fig. 11.

Table 1. Lift coefficient C_l for Aerospatiale A

D_j/c	$B = 0$	$B = 0.5$	$B = 1$	$B = 2$
0.25%	1.578	1.557	1.704	1.929
0.5%	1.578	1.509	1.665	1.951
1%	1.578	1.367	1.394	1.805

Table 2. Drag coefficient C_d for Aerospatiale A

D_j/c	$B = 0$	$B = 0.5$	$B = 1$	$B = 2$
0.25%	0.0189	0.0178	0.0190	0.0188
0.5%	0.0189	0.0169	0.0152	0.0096
1%	0.0189	0.0104	0.0021	-0.011

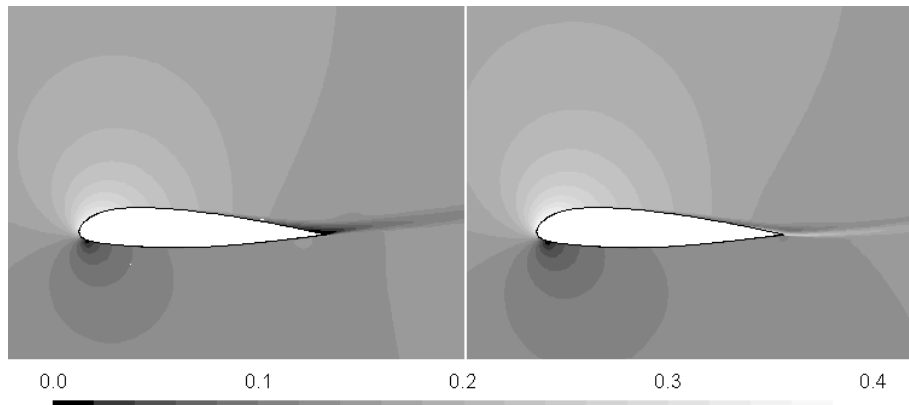


Figure 11. Mach number contours around the clean Aerospatiale A airfoil and airfoil with flow control

For flows over NACA 0012 the Spalart-Allmaras turbulence model was chosen. Computed aerodynamic performances of the clean airfoil are: lift coefficient $C_l = 0.270$, drag coefficient $C_d = 0.0565$ and lift-to-drag ratio $C_l/C_d = 4.77$, while computed results with active

Table 3. Lift coefficient C_l for NACA 0012

D_j/c	$B = 0$	$B = 0.5$	$B = 1$	$B = 2$
0.25%	0.270	0.277	0.403	0.858
0.5%	0.270	0.182	0.420	0.953
1%	0.270	0.038	0.057	1.031

Table 4. Drag coefficient C_d for NACA 0012

D_j/c	$B = 0$	$B = 0.5$	$B = 1$	$B = 2$
0.25%	0.0565	0.0520	0.0628	0.1143
0.5%	0.0565	0.0418	0.0612	0.1274
1%	0.0565	0.0285	0.0310	0.1395

flow control are listed in tabs. 3 and 4. In this case, the desired effect of broadening the sonic bubble along the upper surface and moving the separation point to the trailing edge can only be achieved with the well balanced values of jet diameter B and intensity D_j . Large but weak jets lead to a great deterioration of aerodynamic performances. On the contrary, sufficiently strong jets can boost C_l up to 3-4 times. This is followed by increased C_d up to 2-2.5 times resulting in an overall improved lift-to-drag ratio. Mach number contours for clean and optimal configuration ($B = 2$, $D_j = 0.0025c$) are compared in fig. 12. The favorable effect of active flow control can be presented by comparing the streamlines around NACA 0012 airfoil in the uncontrolled and controlled case, fig. 13. Jet locations are marked with arrows. It is obvious that even serious flow separation can almost completely be avoided.

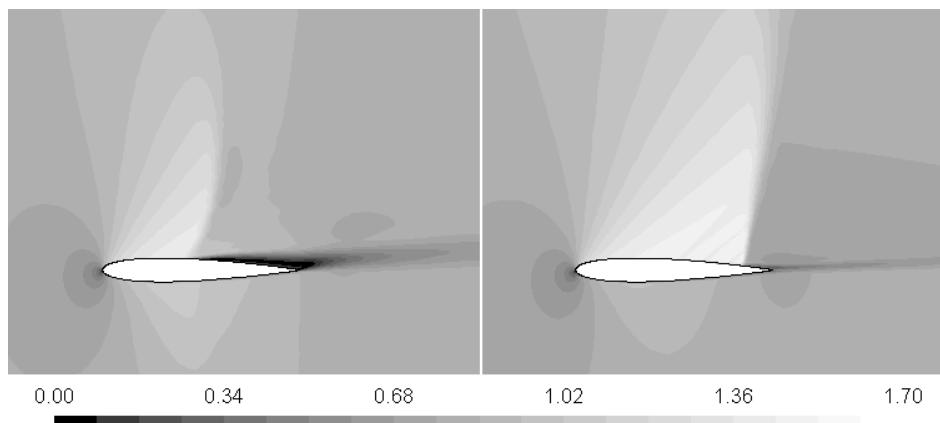


Figure 12. Mach number contours around the clean NACA 0012 airfoil and airfoil with flow control

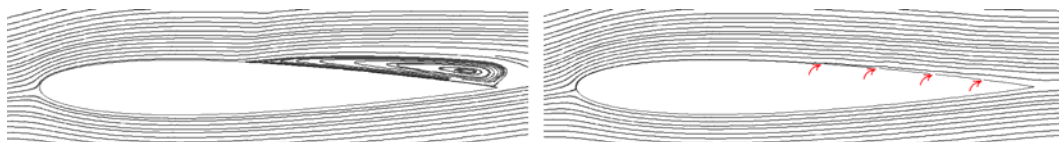


Figure 13. Streamlines around the clean NACA 0012 airfoil and airfoil with flow control

For flows in linear cascades with flow control transition γ - Re_θ turbulence model was employed. In this example somewhat different quantifiers had to be chosen to better represent the benefits of steady blowing. Most important cascade features are inlet and outlet pressures. For that reason, relative pressure difference Δp_{rel} calculated as $\Delta p_{rel} = (p_1 - p_2)/(p_{01} - p_1)$ is listed in tabs. 5 and 6 for compressor and turbine cascades, respectively. In the defined numerical setting of linear cascade the static pressure at the outlet boundary p_2 is the parameter

Table 5. Δp_{rel} for compressor cascade

D_j/c	$B = 0$	$B = 0.5$	$B = 1$	$B = 2$
0.25%	-0.52	-0.49	-0.56	-0.62
0.5%	-0.52	-0.46	-0.54	-0.63
1%	-0.52	-0.41	-0.50	-0.64

Table 6. Δp_{rel} for turbine cascade

D_j/c	$B = 0$	$B = 0.5$	$B = 1$	$B = 2$
0.25%	9.57	9.00	9.94	11.17
0.5%	9.57	8.91	10.04	11.64
1%	9.57	8.84	9.93	12.20

that primarily determines the computational fluid flow and is chosen as the independent variable while the inlet static pressure p_1 is the dependent variable. Computed relative pressure difference of the clean compressor and turbine cascades are $\Delta p_{\text{rel}} = -0.52$ and $\Delta p_{\text{rel}} = 9.57$, respectively. Again, as with the previous example, weak jets (combined with larger orifices) do not increase the absolute value of relative pressure difference while proper combinations of jet parameters can favorably change the flow around the blade and result in an efficiency increase of 20-30%. Qualitative flow representation in the form of Mach number contours of the clean and optimally controlled configurations ($B = 2$, $D_j = 0.01c$) is shown in figs. 14 and 15. Wake consolidation and separation point postponement is obvious.

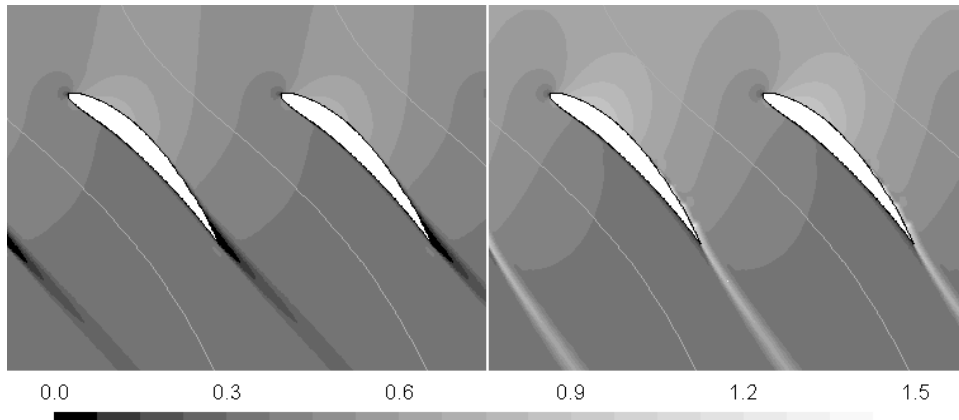


Figure 14. Mach number contours for the uncontrolled and controlled flow in compressor cascade

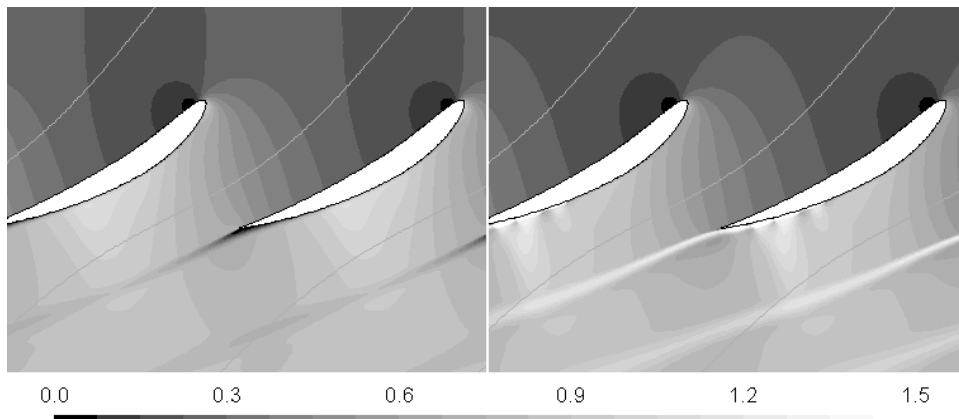


Figure 15. Mach number contours for the uncontrolled and controlled flow in turbine cascade

Conclusions

Different numerical settings for two-dimensional complex boundary layer flows were proposed in the paper. Not all of the results show high accuracy, but various useful conclusions can be extracted, particularly for the purpose of initial, preliminary analyses. Greatest advantages of presented simulations are that they were performed on a personal computer in a couple of hours while not requiring the changes of computational meshes.

Used URANS turbulence models provide results that can significantly differ on clean configurations, especially in high subsonic and transonic regimes. However, given the fact that quite different and distinctive flow fields were investigated, reasonable agreements with experimental results were achieved for clean airfoils without flow control. This fact justified further simulations of boundary layer control by steady blowing. Since jet flows were considered laminar, numerical results on configurations with active flow control differed only slightly indicating that any of the tried turbulence models may be used in the type of problems that involve simulating active flow control by source terms. However, when detailed flow field is to be determined, *i. e.* exact location of the separation point or length of the separation bubble or zone of interaction of shock wave and boundary layer, the user should be most careful. Additional calibration of turbulence models may be necessary as well as additional comparison to experimental results.

Results of the simulations also lead to the conclusion that, by positioning jets along the suction side of the foil and varying their size and intensity, it is possible to change the flow field around the foil, expand sonic zone, move transition point downstream, delay separation, reduce friction drag, *etc.* However, due to great differences in geometry and flow conditions, each case demands a separate analysis and no general conclusions on orifice size and jet intensity can be given.

Presented study can serve as a starting point for various research areas, *e. g.* efficiency increase, decreased noise, and pollutant emission, profile loss decrease, heat transfer enhancement, steadying of the flow (with both static and moving turbomachinery parts), *etc.* It can provide insight into problems that are difficult and expensive to experiment upon. Finally, it can be extended to: three-dimensional analysis to obtain more reliable and accurate results, turbomachinery problems where both stator, rotor, and their interference is taken into account, more detailed studies of active flow control where continuous jets are compared to synthetic ones, *etc.*

Acknowledgment

The research work is funded by Ministry of Education, Science, and Technological Development of Republic of Serbia through Technological Development Project no. 35035.

Nomenclature

a – speed of sound, [ms^{-1}]
 B – jet intensity, [–]
 C_d – drag coefficient, [–]
 C_f – skin friction coefficient, [–]
 C_l – lift coefficient, [–]
 C_p – pressure coefficient, [–]
 CFL – Courant number ($= v\Delta t/\Delta x$), [–]
 c – chord, [m]
 c_p – constant pressure heat capacity, [$\text{Jkg}^{-1}\text{K}^{-1}$]
 D_j – orifice diameter, [m]
 E – total energy per unit mass, [Jkg^{-1}]
 F – force per unit mass, [Nkg^{-1}]
 k – turbulence kinetic energy, [m^2s^{-2}]
 M – Mach number ($= v/a$), [–]
 Pr_t – turbulent Prandtl number, [–]
 p – pressure, [Pa]
 Δp_{rel} – relative pressure difference, [–]

Re – Reynolds number ($= \rho v c/\mu$), [–]
 S – strain-rate tensor, [s^{-1}]
 T – temperature, [K]
 t – time, [s]
 v – velocity, [ms^{-1}]
 x – spatial coordinate, [m]
 y – spatial coordinate, [m]

Greek symbols

α – angle of attack, [$^\circ$]
 γ – intermittency, [–]
 δ_{ij} – Kronecker delta function, [–]
 ε – turbulent dissipation rate, [m^2s^{-3}]
 μ – dynamic viscosity, [$\text{kgm}^{-1}\text{s}^{-1}$]
 ν – kinematic viscosity, [m^2s^{-1}]
 ρ – density, [kgm^{-3}]
 ω – specific turbulent dissipation rate, [s^{-1}]

References

- [1] Dey, J., Narasimha, R., Integral Method for the Calculation of Incompressible Two-Dimensional Transitional Boundary Layers, *J. of Aircraft*, 27 (1990), 10, pp. 859-865
- [2] Schlichting, H., Gersten, K., *Boundary Layer Theory*, Springer, Berlin, 2000
- [3] Rodi, W., DES and LES of Some Engineering Flows, *Fluid Dynamics Research*, 38 (2006), 2-3, pp. 145-173
- [4] Qui, L., *et al.*, Airfoil Profile Optimization of an Air Suction Equipment with an Air Duct, *Thermal Science*, 19 (2015), 4, pp. 1217-1222
- [5] Chen, W-L., *et al.*, Numerical Investigation of Steady Suction Control of Flow around a Circular Cylinder, *J. of Fluids and Structures*, 59 (2015), Nov., pp. 22-36
- [6] Genc, M. S., *et al.*, Performance of Transition Model for Predicting Low Re Airfoil Flows without/with Single and Simultaneous Blowing and Suction, *European Journal of Mechanics – B/Fluids*, 30 (2011), 2, pp. 218-235
- [7] ***, ANSYS Fluent Theory Guide, ANSYS, Inc., Canonsburg, Penn., USA, 2015
- [8] ***, ANSYS Fluent Customization Manual, ANSYS, Inc., Canonsburg, Penn., USA, 2015
- [9] Schmidt, S., Thiele, F., Detached Eddy Simulation of Flow around A-Airfoil, *Flow, Turbulence and Combustion*, 71 (2003), 1-4, pp. 261-278
- [10] Holst, T., Viscous Transonic Airfoil Workshop Compendium of Results, *J. of Aircraft*, 25 (1988), 12, pp. 1073-1087
- [11] Harris, C., Two-Dimensional Aerodynamic Characteristics of the NACA 0012 Airfoil in the Langley 8-Foot Transonic Pressure Tunnel, NASA-TM-81927, 1981
- [12] Schlichting, H., Cascade Flow Problems, AGARD-R-93, Feb., 1957
- [13] Collis, S. S., *et al.*, Issues in Active Flow Control: Theory, Control, Simulation and Experiment, *Progress in Aerospace Sciences*, 40 (2004), 4-5, pp. 237-289
- [14] Corke, T. C., *et al.*, Single Dielectric Barrier Discharge Plasma Enhanced Aerodynamics, *Experiments in Fluids*, 46 (2009), 1, pp. 1-26
- [15] Zhang, D., *et al.*, Numerical Investigation of Heat Transfer Performance of Synthetic Jet Impingement onto Dimpled/Protrusioned Surface, *Thermal Science*, 19 (2015), 1, pp. S221-S229
- [16] Huang, L., *et al.*, Numerical Study of Blowing and Suction Control Mechanism on NACA0012 Airfoil, *J. of Aircraft*, 41 (2004), 5, pp. 1005-1013
- [17] Monir, H. E., *et al.*, Tangential Synthetic Jets for Separation Control, *J. of Fluids and Structures*, 45 (2014), Feb., pp. 50-65
- [18] Yousefi, K., Saleh, R., Three-Dimensional Suction Flow Control and Suction Jet Length Optimization of NACA 0012 Wing, *Meccanica*, 50 (2015), 6, pp. 1481-1494
- [19] De Giorgi, M. G., *et al.*, Comparison between Synthetic Jets and Continuous Jets for Active Flow Control: Application on a NACA 0015 and a Compressor Stator Cascade, *Aerospace Science and Technology*, 43 (2015), June, pp. 256-280
- [20] Gmelin, C., *et al.*, Active Flow Control Concepts on a Highly Loaded Subsonic Compressor Cascade: Resume of Experimental and Numerical Results, *J. of Turbomachinery*, 134 (2012), 6, ID 061021
- [21] Svorcan, J., *et al.*, Active Boundary Layer Control in Linear Cascades using CFD and Artificial Neural Networks, *Aerospace Science and Technology*, 39 (2014), Dec., pp. 243-249